Article:

Gardner, R, Piazolo, S orcid.org/0000-0001-7723-8170, Evans, L et al. (1 more author) (2017) Patterns of strain localization in heterogeneous, polycrystalline rocks – a numerical perspective. Earth and Planetary Science Letters, 463. pp. 253-265. ISSN 0012-821X

https://doi.org/10.1016/j.epsl.2017.01.039

Highlights

- Shear zones are difficult to form without a dynamic weakening mechanism
- Dynamic weakening can quickly localize strain into an interconnected weak zone
- Competing weakening and strengthening processes impact shear zone pattern
- Shear zones are dynamic in time and space within a single deformation event
- Finite strain patterns do not fully represent the evolution of a shear zone network

*Manuscript

Patterns of strain localization in heterogeneous, polycrystalline rocks – a numerical perspective

*Robyn Gardner[1], Sandra Piazolo[1,2], Lynn Evans[1,3], Nathan Daczko[1]

[1]Australian Research Council Centre of Excellence for Core to Crust Fluid Systems/GEMOC, Department of Earth and Planetary Sciences, Macquarie University, NSW 2109, Australia.

[2]School of Earth and Environment, University of Leeds, UK.

[3]School of Earth, Atmosphere and Environmental Sciences, Monash University, Clayton, Vic 3800, Australia.

*robyn.gardner@mq.edu.au Phone: 61-2-9850 4728

Abstract

The spatial and temporal patterns of strain localization in materials with pre-existing heterogeneities are investigated via a series of two-dimensional numerical models. Models include (i) a dynamic feedback process, to simulate rheological weakening in response to the transition from non-linear flow (dislocation creep) to linear flow (diffusion creep/grain boundary sliding), and (ii) a time dependent strengthening process, counteracting the weakening process. Different load bearing framework geometries with 20% weak component are used to evaluate the impact of geometry on the strength of the material and its ability to localize strain into an interconnected weak layer (IWL). Our results highlight that during simple shear, if dynamic weakening with or without strengthening feedbacks is present, strain is quickly localized into an IWL, where an increasing proportion of weak material increases the interconnections between the IWLs, thereby increasing the anastomosing character of the shear zones. We establish that not only bulk strain localization patterns but also their temporal patterns are sensitive to the dominance of the weakening or strengthening process. Consequently, shear zones are dynamic in time and space within a single deformation event. Hence, the pattern of finite strain can be an incomplete representation of the evolution of a shear zone network.

Keywords

Anastomosing; shear zone; dynamic weakening; material strength; geometry; weak component

1. Introduction

Strain localization fundamentally controls a material's rheological response to deformation. Shear zone initiation and development is, therefore, widely studied at all scales, from single crystal behaviour to crustal scale high strain zones (e.g. Carreras, 2001). There is well-documented evidence of the major role localization plays in governing important rheological and economic structures (e.g. Bouchot et al., 1989). However, speculation remains regarding the mechanisms and patterns of strain localization, including the influence of rheology and geometry of pre-existing heterogeneities, and the importance of weakening and strengthening processes. For example, field evidence indicates strain concentration is highly variable, from single zones of ultramylonite to mylonite, to anastomosing, that is, interconnected, sets of high strain zones (e.g. Arbaret et al., 2000; Carreras et al., 2010; Svahnberg and Piazolo, 2010). Understanding the underlying principles for this variability will improve our ability to utilize shear zone localization patterns for characterization of material behaviour through time and to model Earth processes.

Rock heterogeneity impacts strength anisotropy, the bulk strength and the evolution of the fabric governing where localization occurs. Heterogeneity results from the (i) strength contrast between the phases (e.g. Dell'Angelo and Tullis, 1996; Handy, 1994; Hansen et al., 2012; Holyoke III and Tullis, 2006); (ii) interconnectivity, and geometric patterns of weak components (e.g. Gerbi, 2012; Gerbi et al., 2016; Treagus, 2002; Tullis et al., 1991); (iii) pre-existing fabrics, for example, foliation (e.g. Montési, 2013; Rennie et al., 2013) and brittle fractures (e.g. Segall and Simpson, 1986); (iv) volume fraction of weak components (e.g. Handy, 1994; Shea and Kronenberg, 1993; Takeda and Griera, 2006; Treagus, 2002); and (v) deformation mechanisms active in each phase (e.g. Dell'Angelo and Tullis, 1996; Holyoke III and Tullis, 2006).

Strength anisotropy can also evolve by (i) fluid ingress and egress, with or without reactions, creating weaker phases (e.g. Finch et al., 2016; Holyoke III and Tullis, 2006), (ii) changes in temperature, perhaps due to shear heating (e.g. Hobbs et al., 2008; Platt, 2015; Poulet et al., 2014), and/or (iii) recrystallization, causing grain size reduction (e.g. Drury, 2005; Warren and Hirth, 2006) and/or grain coarsening (e.g. De Bresser et al., 1998). Both strengthening and weakening by grain size reduction and growth processes (e.g. Herwegh and Berger, 2004) and water transfer (Finch et al., 2016) have been shown to occur simultaneously in a shear zone. Such coupled and competing processes are known to be important in the Earth's crust, changing the underlying deformation processes as the balance between the processes changes (e.g. Chester, 1995; De Bresser et al., 1998).

Numerical models of evolving strength anisotropy due to grain size changes have been used to explore strain localization. Jessell et al. (2005) implement grain size reduction and growth processes resulting in rheological softening and hardening, respectively. In contrast, Cross et al. (2015) use a grain size paleopiezometer to drive the balance between grain size growth and reduction to a steady state grain size, while Herwegh et al. (2014) implement a dynamic transition between grain size insensitive and sensitive flow regimes using a paleowattmeter. Other authors (e.g. Jessell et al., 2009; Mancktelow, 2002; Takeda and Griera, 2006) have implicitly modelled strength variation using viscosity as a proxy for grain size.

In this contribution, we take a numerical approach and investigate the local dynamic feedback between weak and strong components, using stress dependent weakening and time dependent strengthening as a proxy, rather than explicitly defining a particular strengthening or weakening process. We examine how this dynamic feedback process can readily cause an initially load bearing framework (LBF), where the weak phase is surrounded by a strong matrix, to form an interconnected weak layer (IWL) parallel to the shear plane. In contrast to Handy (1994), who used the IWL and LBF as end member geometries, the numerical models used here show a dynamic feedback process can readily create an IWL from a LBF. We find the IWLs interconnect where the weakening process is widespread, that is, the anastomosing character of the shear zones increases. Even though the processes responsible for weakening and strengthening may operate at the grain scale, our model describes patterns that can be applied up to km-scale localization.

2. Numerical set-up

2.1. General model

Elle, an open source numerical simulation platform (Bons et al., 2008), is used to model deformation of a two-dimensional structure undergoing dextral simple shear. In the Elle platform multiple processes may act sequentially upon the numerical 2D structure (Supp. Fig. 1a). Here, processes include viscous deformation and/or rheological weakening and/or rheological hardening. The viscous deformation of the model is handled in the finite element method (FEM) code, Basil (Houseman et al., 2008). The 2D structure consists of two layers of information. Layer 1 records polygon geometry (Fig. 1a(i)) where each polygon is defined by a closed loop of boundary nodes connected by straight segments (Supp. Fig. 1b). Physical properties including viscosity pre-factor, viscous flow law are defined for each polygon. Cumulative and instantaneous strain and stress are recorded as the simulation progresses. In contrast to many previous applications of the Elle platform (e.g. Llorens et al., 2016; Piazolo et al., 2002), each polygon represents an area of similar physical properties rather than a specific grain, such that straight segments between boundary nodes should not be considered as grain boundaries. Layer 2 is an initially 100 x 100 square grid mesh of unconnected nodes or material information points (Supp. Fig. 1b). In this implementation, the Layer 2 of unconnected nodes provides passive markers of the deformation field as the model run progresses (e.g. Jessell et al., 2009).

A complete simulation includes defining a starting polygon geometry or rock structure, then cycling the rock structure through the series of processes that includes the Basil deformation step, to a user defined incremental strain, and may include none, one, or both of the two optional dynamic rheological processes (i.e. weakening, hardening, see Supp. Fig. 1a) until the desired finite shear strain is reached.

In the simulations presented here, a full iteration of the Elle cycle includes passing the 2D structure to the FEM code Basil (Houseman et al. 2008) where the Layer 1 polygons are triangulated into a finer mesh for the FEM deformation step. Dextral simple shear is applied, using boundary conditions of constant displacement of +0.025 (at the top boundary) and -0.025 (at the bottom boundary). Boundaries are defined to be periodic in both the x and y direction. In this implementation Basil uses dimensionless variables and assumes an incompressible medium with viscous behaviour described by the constitutive relationship:

$$\tau_{ij} = 2\eta\dot{\varepsilon}_{ij} = \eta\left[\frac{\partial u_i}{\partial x_j} + \frac{\partial u_j}{\partial x_i}\right]$$

Where τ_{ij} is the deviatoric stress tensor, $\dot{\varepsilon}_{ij}$ is the strain rate tensor, u is the velocity in the x or y direction, η is the effective viscosity defined by:

$$\eta = \frac{1}{2}\eta^{*}\dot{E}^{\left(\frac{1-n}{n}\right)}$$

where $\dot{E}$ is the second invariant of the strain rate tensor, *n* is the stress exponent and η^{*} is a viscosity pre-factor. The FEM code Basil, calculates a converged solution based on the constitutive relationships, boundary conditions and the Layer 1 polygon geometry and properties input from Elle. For a full discussion of the Basil formulation, please see Houseman et al. (2008).

The solution calculated by Basil is passed back to Elle where the geometry and values (e.g. stress) of Layer 1 polygon mesh and the position of the Layer 2 nodes are both updated. The Elle control script then calls the next process to act upon the structure (Supp. Fig. 1a). To simulate the processes of weakening and strengthening during deformation, Elle calls each process in turn, at each time step (Jessell et al., 2001; Piazolo et al., 2010), depending on the chosen simulation set, as outlined below.

Within Elle, the initial viscosity pre-factor and stress exponent are defined on the Layer 1 polygons, hence, it is possible to define geometries with differing properties on each polygon. The properties are dimensionless, based on the unit cell. For the presented numerical models, we have defined a load bearing framework (LBF) where approximately 20 area% is rheologically weak, with a relatively low viscosity pre-factor of 1, while the majority of the polygons are stronger, with viscosity pre-factor of 5. We present results using five different initial geometries (Fig. 1a (ii) – (iv)); random, clusters, rings and two with stripes, the first where the stripes are parallel to the shear plane, here called horizontal stripes, and the second where the stripes are perpendicular to the shear plane, here called vertical stripes. We run four sets of simulations which differ in the complexity of dynamic feedbacks simulated. Simulation set I does not involve any dynamic feedbacks, hence no rheological changes occur throughout the deformation. In contrast, simulation sets II and III involve dynamic weakening (Fig. 1c) while in simulation set IV both weakening and strengthening are modelled (Fig. 1d). A summary of the simulations undertaken is included in Table 1 and the dynamic simulations are visually represented in Figure 1b.

	Simulation Set Number	Geometry	Flow Regime (n)	Weakening Stress threshold (σ_{Thr})	Strengthening Age threshold (A_{Thr})
Static	I	Horizontal stripes	n=1	NA	NA
		Vertical stripes			
		Cluster			
		Ring			
		Random			
		Horizontal stripes	n=3		
		Vertical stripes			
		Cluster			
		Ring			
		Random			
		Horizontal stripes	Mixed: n = 1 or 3		
		Vertical stripes			
		Cluster			
		Ring			
		Random			
Dynamic	II	Horizontal stripes	Mixed: n = 1 or 3	6.0	NA
		Vertical stripes			
		Cluster			
		Ring			
		Random			
	III	Cluster	Mixed: n = 1 or 3	4.0	NA
				4.5	
				5.0	
				5.5	
				6.0	
				6.5	
	IV	Cluster	Mixed: n = 1 or 3	4.0	5
				4.0	10
				4.0	15
				4.0	20
				5.0	5
				5.0	10
				5.0	15
				5.0	20
				6.0	5
				6.0	10
				6.0	15
				6.0	20

Table 1. Summary of numerical simulation sets providing parameters of individual simulations.

All simulations are run to 80 simulation steps, representing finite shear strain (γ) of 2. One simulation set is additionally run to a finite shear strain of 2.75 to allow assessment of the effect of higher finite strain on material strength behaviour. Stress

(σ) and incremental strain values (ε_{Incr}) are calculated from velocity gradients during the deformation step in Basil (for details, see Houseman et al., 2008). Accumulated strain is calculated by the accumulation of incremental strains throughout the progressive deformation. These values are collected on both the Layer 1 polygons and Layer 2 unconnected nodes at each time/deformation step.

2.2. Rheological weakening and strengthening: Rational and numerical implementation

The dynamic simulations (sets II, III and IV) use two dynamic rheological processes, one simulating weakening and the second simulating additional strengthening (Fig. 1b, c and d).

The dynamic weakening process simulates the transition from a relatively strong (η^* = 5), non-Newtonian (n = 3), grain size insensitive flow regime to a relatively weak (η^* = 1), Newtonian (n = 1), grain size sensitive flow regime (Fig. 1b, red arrows and c). The rationale underlying this weakening process is that it is now well established that during dynamic recrystallization, grain size reduction is stress dependent (Twiss, 1977). If the grain size is sufficiently decreased at high stresses, the flow law switches from the dislocation creep regime to the diffusion creep regime. This results in a switch in rheological behavior from a high viscosity material with a stress exponent of 3, to a low viscosity material with a stress exponent of 1 (Ashby, 1972; Smith et al., 2015 and references therein). Over the last two decades, there has been a marked increase in the number of field examples documenting pronounced weakening of rock strength with strain localization due to a switch from dislocation creep regime to diffusion creep/grain boundary sliding (GBS) processes caused by grain size reduction (Fig.1b; Barnhoorn et al., 2005; Fliervoet et al., 1997; Smith et al., 2015). Numerically, the transition from strong to weak is triggered according to the stress experienced by each polygon, with a threshold (σ_{Thr}) defining the stress value at which a polygon is weakened. At low σ_{Thr} extensive weakening occurs.

The dynamic strengthening process, used only in simulation set IV, simulates the opposite effect to the weakening process. That is, the transition of the material strength from relatively weak to relatively strong (Fig. 1b, blue arrows and d). Viscosity pre-factor and stress exponent increase, from $\eta^* = 1$ to $\eta^* = 5$ and n = 1 to n = 3, respectively. This simulates the physical effect of a fine grained, polycrystalline rock undergoing grain growth causing increased grain size. This results in a transition from weak, grain size sensitive flow with n = 1, to a strong, grain size insensitive flow with n = 3 (Fig. 1b) (e.g. De Bresser et al., 2001). The grain size increase is time dependent where, with more time, the likelihood of a grain being large enough to switch to grain size insensitive deformation increases. The rate at which grain growth occurs is dependent on the mineral phase, temperature, grain size and fluid availability (Piazolo et al., 2002 and references therein). Accordingly, in our implementation, the timing of the rheological transition to higher viscosity and higher stress exponent depends on the duration (i.e. the numerical "age" or number of time steps) of the polygons being weak, with a threshold (A_{Thr}) defining the number of time steps after which the polygon is strengthened. That is, a low A_{Thr} indicates efficient strengthening.

2.3. Analysis of numerical simulations results: Material strength

After each numerical time step, stress on the deformed Layer 2 100 x 100 unconnected node mesh is processed in Matlab®, where it is interpolated onto a regular grid. The volume under this stress surface (that is, the double integral of the stress values) is taken to be the bulk material strength for that step (Houseman et al., 2008). For each model these values are graphed for the duration of the model run, that is, to γ of 2.To verify the integrity of the models, simulated material strengths are compared to the two theoretical end-member bounds, iso-stress and iso-strain bounds (for details see Appendix 2).

3. Results

3.1. Simulation set I: no dynamic feedback – Impact of pre-existing geometry on material strength and strain localization

Simulation set I includes three series of models using the five different starting geometries (Fig 1a(ii) – (vi)), varying only the stress exponent between the series. No dynamic feedback processes are used, so the polygon viscosities do not vary from the initial volume fraction of 20% weak material ($\eta^* = 1$). The first series uses only Newtonian flow (n = 1), the second non-Newtonian flow (n = 3), and the third, a mixed Newtonian and non-Newtonian flow, where Newtonian flow is applied to the weak component and non-Newtonian flow to the strong component. Simulation results (Fig. 2a) indicate that Newtonian flow for the whole model geometry results in a material that is much weaker than the non-Newtonian and mixed flow regime geometries. The mixed flow regime geometries (Fig. 2a, dotted lines) are weaker, but relatively similar to the pure non-Newtonian rheology, except for the horizontal striped geometry which is considerably weaker and closer to the Newtonian rheology in strength. For all geometries the strain is concentrated into the weak areas, though no additional IWLs form (Supp. Fig. 3).

Of the five geometries the horizontal striped geometry is by far the weakest as it is effectively a pre-existing IWL. Random, cluster, ring and vertical striped geometries for each series all fall within a narrow band and all display some curvature, possibly due to rotation of the weak geometry as the deformation progresses. The difference in strength between the horizontal striped and the other geometries is ~ 0.5 (in non-dimensional strength units) for both the Newtonian and non-Newtonian only flow regimes, while for the mixed regime this range is over double this, at ~ 1.3, indicating a wider range of strength variability in the mixed flow regime models.

Vertical stripes display the maximum strength of all the geometries tested. Strength increases as the stripes rotate towards an angle of 45° to the shear direction (Fig. 2a). Maximum strength is reached at γ of ~ 0.85 and maintained until γ of ~ 1.45, where the stripes have rotated to be < 45° to the shear direction (Fig. 2a, inset images). Material strength then gradually reduces as the stripes further rotate towards the horizontal.

3.2. Simulation set II: dynamic rheological weakening - Impact of geometry and weakening on material strength and strain localization

In simulation set II, we use the same starting geometries (Fig. 1a(ii) – (vi)) and the mixed Newtonian, non-Newtonian flow regime as the third series in simulation set I. In addition, the weakening dynamic feedback process (Fig. 1c) is implemented with a stress threshold (σ_{Thr}) of 6.0. Similar to set I results, the horizontal striped geometry is much weaker than the other geometries (Fig. 2b) due to the pre-existing IWLs parallel to the shear direction (Fig. 3a). No additional polygons were weakened throughout the horizontal striped geometry simulation as the stress in the stronger polygons did not exceed the threshold for weakening.

In contrast to simulation set I where no additional IWLs are formed (Supp. Fig. 3), the stress in set II initially concentrates irregularly in high viscosity areas at the boundary of pre-existing weak polygons. Any polygon that exceeds $\sigma_{Thr} = 6.0$ is converted to a weak polygon. In this way, the IWLs form by concentrating stress on the edge of a weak geometry polygon and then propagating with low stress, high strain polygons behind it. Initially this occurs parallel to the shear plane. Once an IWL is formed, stress then concentrates on the high viscosity edges of the IWL causing it to gradually widen if the stress is high enough to trigger a switch in rheology (Fig. 3, bars on accumulated strain graphs). The IWL width stabilises once the stress concentrated in the polygons on the edge of the IWL no longer exceeds the threshold. Two movies depicting the evolution of stress and incremental strain forming an IWL for the vertical stripes model, are included in the Supplementary Data (Movie 1 and 2). These movies also show the widening of the IWL.

Similar to set I, the random, cluster and ring geometries all show very similar material strength behaviour to each other (Fig. 2b). With increasing strain, strong polygons exceed the stress threshold and are weakened. This successively increases the area of weak component, gradually reducing the overall material strength (Fig. 2b). The accumulated strain shown in the deformation grids for these geometries (Fig. 3c, d and e) shows the weak polygons occur in a layer parallel to the shear plane, and that strain localization, is established by γ of 1. The IWLs are narrow at γ of 1, having been formed by just a few interconnected weak polygons, but, by γ of 2 the weak zones are wider and well established (Fig. 3c, d and e, bars to the right of the graphs).

Material strength of the vertical striped geometry material (Fig. 2b) initially increases as the stripes rotate, in a similar manner to the simulation set I runs. However, in this set, as the peak material strength is reached, strong polygons begin to exceed the stress threshold and become weak causing the initiation of an IWL (Fig. 2b, insets), and a steep reduction in the material strength. As the strain is further localized into the IWL (Fig. 3b), the material strength evolves to a value similar to the random, cluster and ring geometries (Fig. 2b).

The incremental strain plots (Fig. 3, left hand side) show where the strain has localized at a specific strain value. Once an IWL is established, most strain is concentrated into the IWL. However, the pre-existing weak geometry still concentrates some strain, though this is much reduced unless that geometry falls within the IWL (Fig. 3b-d, incremental strain plots at γ of 2 show traces of the original weak geometry). The accumulated strain shown in the deformation grid images shows the deformation as would be seen in a rock outcrop (e.g. Supplementary Fig. 4). The pre-existing weak geometry is still obvious and can be seen to deflect into the IWLs. This is particularly obvious in the vertical striped geometry (Fig. 3b), but can also be seen in the cluster, ring and random geometries (Fig. 3c, d and e). Minor variability in the material strength (Fig. 2b) is due to the impact of the changing and rotating geometries of the weak component.

3.3. Simulation set III: dynamic rheological weakening - Impact of the stress threshold on strain localization

In simulation set III, we investigate the impact of varying the stress threshold at which weakening occurs, on strain localization and thereby, the high strain zone geometry. We use the cluster geometry (Fig. 1a (v)) with the dynamic weakening process (Fig. 1c), and vary σ_{Thr} to 4.0, 4.5, 5.0, 5.5, 6.0 and 6.5 in separate runs. Since experiments are run at the same boundary conditions, decreasing the stress threshold results in an increase in the area percent that is effected by weakening (i.e. high versus low amount of weakening at σ_{Thr} to 4.0 versus 6.5, respectively).

For low values of σ_{Thr} (4.0 and 4.5), a high percentage of strong polygons immediately exceed the threshold and are converted to the weak phase – this is reflected in an initial sharp strength drop (Fig. 4, σ_{Thr} = 4.0 & 4.5 lines) and the η^* plots (Fig. 5a and b) where the material essentially becomes a weak phase supporting (WPS) material. The weak polygons form the major proportion of the material (Fig. 4b). Strain is accumulated in this extensive network of weak polygons and, for σ_{Thr} of 4.0 no distinct IWLs form (Fig. 5a). Isolated areas of stronger component remain, and rotate as the simulation continues. Wide, interconnected zones of weakness form for σ_{Thr} of 4.5, as shown by the wide peaks in the accumulated strain graph (Fig. 5b). At the same time, a few areas of high viscosity, stronger component, remain which exhibit very little strain (Fig. 5b).

Where the σ_{Thr} is 5.0 and 5.5 (Fig. 4, σ_{Thr} = 5.0 & 5.5 lines), the initial sharp decrease in strength is smaller than for the very low σ_{Thr} models, with greater than 50% of the material remaining strong. The material remains a LBF (Fig. 4b, 5c and d, η^* plots). After the initial drop, the material strength continues to gradually decrease as additional strong polygons are converted to weak polygons allowing the weak component to interconnect into IWLs, parallel to the shear direction (Fig. 5c and d). For σ_{Thr} of 6.0 there is no sharp initial reduction (Fig. 4, σ_{Thr} = 6.0 line), but the gradual conversion of strong polygons to weak, similarly causes the formation of two IWLs parallel to the shear direction. In these three models (σ_{Thr} of 5.0, 5.5 and 6; Fig. 5c, d and e, respectively), by γ of 1, the weak component has created multiple IWLs.

Peaks in the accumulated strain graphs indicate the location of the IWLs, with bars to the right indicating their widths. The σ_{Thr} of 5.5 accumulated strain graph (Fig. 5d) shows the strongest strain localization in the top IWL.

Where the σ_{Thr} is very high, at 6.5 (Fig. 4, σ_{Thr} = 6.5 line), very few polygons exceed the threshold to be weakened, causing the bulk strength to be unchanged during the simulation. This is also reflected in the accumulated strain plots (Fig. 5f), where strain continues to concentrate into the pre-existing weak geometry, and the accumulated strain graph which shows low peaks (Fig. 5f), and no IWL formation. At γ of 2, a few polygons have been converted to the weak component and have started to connect, so an IWL parallel to the shear direction may occur at higher γ values.

As the σ_{Thr} is reduced, allowing more weakening, IWLs become wider and more numerous, with interconnecting branches via the pre-existing weak geometry (Fig. 5, bars to the right of the accumulated strain graphs).

3.4. Simulation set IV: dynamic weakening and strengthening – Impact of the relative activity of weakening versus strengthening

In simulation set IV, we add a dynamic strengthening process (Fig. 1d) to investigate the impact of including both weakening and strengthening processes on strain localization. We use only the cluster geometry (Fig. 1a(v)) with dynamic weakening (Fig. 1d) implemented at σ_{Thr} of 4.0, 5.0 and 6.0 (a subset from simulation set III). The dynamic strengthening process (Fig. 1d), is based on an age threshold (A_{Thr}) varied through the following values: 5, 10, 15 and 20. At the start of the model run, the age on the pre-existing weak polygons and any polygons weakened in the initial step are set to random values between 0 and the A_{Thr}. The age is then incremented on each step.

All models show that IWLs readily form, and similar to simulation set III, as σ_{Thr} is decreased, that is, greater weakening occurs, more IWLs form (Fig. 6). As A_{Thr} is decreased, that is, more strengthening occurs, the number of IWLs decreases (Fig. 6 and 7a). Strain is highly concentrated into the IWL once it has formed and some gradual widening of the IWLs can be seen (Fig. 7a, bars to the right of the accumulated strain graphs), though this is not as evident as for simulation sets II and III.

The incremental strain images indicate that not all parts of the IWLs are active at the same time (Fig. 7, Supplementary movies 3-7). As polygons are strengthened, strain is no longer localized into those polygons (e.g. Fig. 7a black arrows), though this may be short-lived where the polygons fall within an IWL, as they may be re-weakened at the next step. In this way, the polygons within the IWL oscillate between being weak and strong based on the A_{Thr}. Incremental strain in the IWLs is dependent on the area of weak polygons present at that time step. This is highlighted in Figure 7b where the highest strains ($\varepsilon_{Incr} > 0.06$) occur intermittently across the three IWLs once these have formed, after γ of 0.125 (Fig. 7b(i)). See also Supplementary movie 7 for all steps for Figure 7b.

Addition of the strengthening process causes the materials to be stronger than the materials with no dynamic strengthening (Fig. 8, compare with thick black lines). Variation of the strengthening process causes little difference to the bulk strength for LBF materials, though increased strengthening (i.e. lower A_{Thr}) causes more cyclic behaviour in the model. For example, in all $A_{Thr} = 5$ models, the material strength is cyclic (Fig. 8a to c, dotted lines). As the deformation continues for all A_{Thr} in σ_{Thr} of 5.0 and 6.0, the overall material strength gradually weakens to a γ of 1 then gradually strengthens to a γ of 2 (Fig. 8b and c). This corresponds to an initially decreasing, then increasing proportion of strong polygons. Some of the IWLs that were initially formed become dormant from γ of 1 (Fig. 7c, black arrow and Supplementary movie 3a). Supplementary movie 3 shows that the top narrow IWL, after initial formation has progressively reducing strain concentration with time. Continuing this dynamic model to γ of ~ 2.75 (Supplementary movie 3a) shows the IWL becomes dormant and no longer concentrates any strain by γ of ~ 2.5. This indicates a balance between the strengthening and weakening processes is not established, and the strengthening process dominates the weakening process later in the model.

The same cluster geometry was run multiple times at σ_{Thr} of 6.0 and A_{Thr} of 5, with all initial ages set to zero (Fig. 9). From this initially identical setup, minor differences have occurred between the models during the deformation and dynamic feedback steps. In each run, this causes different polygons to concentrate stress, and thereby be converted to weak material. Figure 9a shows that very little weak material (0.74% area) is needed to initiate an IWL, if the material lies in a line parallel to the shear plane. By contrast, in the second model run (Fig. 9b) the distribution of weak polygons did not allow an IWL to form, even where the model was run to gamma of 2.0. The ability of a material to develop effective IWLs is highly dependent on the local geometry of soft versus hard components.

4. Discussion

4.1. General validity of the numerical model

Confidence in the numerical model presented is provided by (i) the similarity of the results to experimental (e.g. Dell'Angelo and Tullis, 1996; Holyoke III and Tullis, 2006) and numerical tests (e.g. Cook et al., 2014; Gerbi et al., 2015) showing the horizontal geometry is weakest; (ii) the experiments of Shea and Kronenberg (1993) who show, similar to our vertical striped geometry, that a 45° angle of the weak phase to the shear direction is the strongest; (iii) all model strengths fall between the calculated iso-stress and iso-strain bounds (e.g. Treagus, 2002) with the horizontal geometry very close to the iso-strain boundary (Supplementary Fig. 2a); (iv) strain is concentrated into the weak polygons (e.g. Handy, 1994); (v) strain weakening and evolution of the IWLs in our models comparable to experiments by Holyoke III and Tullis (2006), Dell'Angelo and Tullis (1996) and Shea and Kronenberg (1993).

Addition confidence for the model is provided by Gerbi et al. (2016) who show interconnected micro shear zones typically form at sites of high stress, and that weak zone rheology depends on the local conditions specific to the weak zone.

4.2. Influence of geometry on material strength

Numerous authors have attempted to quantify the impact of weak components on the aggregate strength of a material, with for example, the inclusion of a constant to represent the geometry (e.g. Bons et al., 2008, H value; Treagus, 2002, p value). However, Gerbi (2012) suggests such a constant is difficult to establish, and this is in agreement with our simulations (Fig. 2 and 3). As the deformation continues, the geometry changes, thereby changing any geometry based constant, though this may approach a steady state at higher strains if the weakening processes dominate.

Simulation sets I and II (Fig. 2a and b) show the horizontal geometry is much weaker than the other geometries as the pre-existing geometry acts as an IWL to concentrate strain. Our dynamic simulation set II (Fig. 2b) displays that as the IWLs form in the other geometries, the material strength evolves towards that of horizontal geometry, irrespective of the initial weak geometry, confirming that layers of weak components parallel to the shear direction represent the weakest geometry (e.g. Cook et al., 2014; Dell'Angelo and Tullis, 1996; Gerbi et al., 2015; Holyoke III and Tullis, 2006).

These models also indicate that the presence, or absence, of an IWL parallel to the shear plane (i.e. horizontal striped geometry), and the proportion of weak component in the material are the most important determinants for material strength and strain localization. Increasing the proportion of weak component increases the likelihood of weak components being able to interconnect to form an IWL. Once an IWL has formed, strain is concentrated in the weak zone and deformation outside the weak zone is significantly reduced. Hence, the deformation within the wall rock surrounding a shear zone can provide indications of the pre-localization history. This also indicates that the pre-existing weak component geometry is important initially, in the deformation process, but that after the IWL forms it becomes less important.

4.3. Influence of flow regime and dynamic weakening on material strength and strain localization

Many previous numerical experiments (e.g. Cross et al., 2015; Jessell et al., 2009; Jessell et al., 2005; Mancktelow, 2002) have specified the flow regime as either linear or non-linear with no allowance for dynamic transition from one regime to the other. Mancktelow (2002) and Jessell et al. (2005) both suggest strain localization is enhanced in non-linear flow regimes. This situation corresponds to, and agrees with, our single flow regime, static simulation set I models. In our mixed flow regime models, we have defined our weak component to deform in a Newtonian flow regime (Fig. 2a, dotted lines), as the Newtonian materials are much weaker than the non-Newtonian materials (Fig. 2a). This results in a larger difference between the horizontal striped geometry strength and the other geometries (Fig. 2a, dotted lines), than is seen for the single flow regime models (Fig. 2a, solid and dashed lines). This suggests the geometry in the mixed flow regime allows greater strength variability than in the Newtonian and non-Newtonian only flow regimes, allowing the weakening impact to be accentuated. This is in agreement with conclusions derived from analysis of rocks that are interpreted to have undergone a weakening process (e.g. Fliervoet et al., 1997; Smith et al., 2015).

Simulation set I, where no dynamic simulation was active, failed to form additional IWLs (Supp. Fig. 3). Our dynamic simulation sets II, III and IV show that dynamic feedbacks causing rheological weakening allow IWLs to readily form. Our additional model in simulation set IV (Fig. 9) shows that a fortuitous arrangement of weak polygons, forming due to the dynamic weakening process, at only 0.74 area% weak component, can cause an IWL to form.

4.4. Influence of temperature and shear strain rate on patterns of strain localization

Experiments on individual minerals, at specified temperature and shear strain rates, have determined the grain size and shear stress relationships, which govern whether a material deforms by dislocation creep or diffusion creep/GBS (Fig. 1b; see Rybacki and Dresen, 2004 for examples of these diagrams for plagioclase). Figure 1b summarizes the models in this grain size and shear stress space. Simulation sets II and III provide a proxy for weakening behaviour at single, and multiple, temperature and shear strain rates, respectively. Simulation set IV provides a proxy for both weakening and strengthening behaviour at multiple temperature and shear strain rates (Figure 1b).

In our dynamic models, decreasing σ_{Thr} increases the amount of weakening occurring. Where this feedback process is used on its own (simulation sets II and III), we suggest this corresponds with a permanent shift to a weaker state, such as that seen in polymineralic rocks where a second component can inhibit grain growth processes, for example, by Zener pinning (e.g. Brodhag et al., 2011; Warren and Hirth, 2006).

Our simulation set III, where weakening is extensive (σ_{Thr} is low), shows that at higher temperatures and/or lower strain rates, where the overall material is weaker, a higher percentage of the material transitions to Newtonian flow, causing increased numbers of interconnected IWLs to form. At lower temperatures and/or higher strain rates, the opposite is true; fewer, less interconnected, IWLs concentrate the strain. This is in agreement with field evidence of anastomosing shear zones which are commonly seen at middle to lower continental crust levels, that is, at amphibolite to granulite facies conditions (e.g. Arbaret et al., 2000, 550-650 °C and 0.9 to 1.0 GPa; Carreras et al., 2010, 400-600 °C and ~ 300 MPa; Svahnberg and Piazolo, 2010, 675-700°C and ~ 400 MPa). At lower temperatures, more restricted shear zones form (Hanmer, 1988). Arbaret et al. (2000) found three sets of anastomosing shear zones in the Kohistan arc, NW Pakistan. Of interest here are their set 2 and 3 shear zones. Set 2 shear zones are densely spaced and interconnected, and formed at upper amphibolite facies, while set 3 shear zones are far fewer, thicker and formed at lower amphibolite facies. As a second example, Carreras et al. (2010) document a shear zone in the Rainy Lake Zone, Canada, with an extensive anastomosing geometry where it falls within amphibolite facies terrane, but it is reduced to two major shear zones where it falls within the greenschist facies terrane. Both of these scenarios represent concentration of strain into a narrower zone at lower temperature.

These natural examples correlate well with our models in simulation set III. Results show that, with reduced weakening (higher σ_{Thr}), bulk strength is stronger and strain localizes in fewer IWLs than at lower σ_{Thr}. Hence, at lower temperatures or increased strain rate, strain localizes into fewer IWLs. Conversely, at higher temperatures, or slower strain rates strain localises into increased numbers of interconnected IWLs forming anastomosing shear zone networks. This result also correlates to those of Chester (1995), who, in contrast to our models, worked in the brittle regime, but found that fault zones weaken as they widen.

4.5. Influence of the relative activity of weakening and strengthening process on patterns of strain localization

Competing processes are known to be important in the Earth's crust (e.g. Chester, 1995; De Bresser et al., 1998; Finch et al., 2016). Where both the weakening and strengthening feedback processes operate (simulation set IV, Fig. 6), we suggest this corresponds to monomineralic rocks where counteracting processes governing weakening and strengthening operate. Examples of these counteracting processes include grain size decrease versus increase (De Bresser et al., 1998; Hansen et al., 2012) and hydration versus dehydration (Finch et al., 2016). Our results show as the influence of weakening increases, the zones of strain localisation become less focused, and as the influence of strengthening increases the zones become more focused (Fig. 6).

Our simulation set IV (Fig. 7), in agreement with Jessell et al. (2005), shows that in a dynamic regime, with both strengthening and weakening processes, the localization of strain is not stable over time (Fig. 7, Supplementary movies 3-7), and that once IWLs have formed, these too may or may not continue to localize strain (Supplementary movie 3). Graphs of all A_{Thr} values show an underlying curvature, with increasing material strength towards γ of 2 (Fig. 8). This suggests the weakening process initially dominates as the material gradually weakens, but as the deformation progresses the balance between the competing processes is shifted to domination by the strengthening process. This is more pronounced as the amount of weakening decreases (Fig. 8, as σ_{Thr} changes from 4.0 to 6.0), which suggests, with less weakening, the balance between the two dynamic processes moves more quickly towards the strengthening process, and the shear zones (our IWLs) will become dormant more quickly. This could be extrapolated to suggest at lower temperatures and/or faster strain rates the strengthening mechanism will dominate, thereby gradually turning off the shear zones. That is, the faster the shear zones form, or the lower the temperature, the quicker they are turned off and strain is localised elsewhere.

In our simulations, the accumulated strain maps (Figs. 3, 5, 6 and 7a) represent the total deformation experienced. In a field outcrop, only the total strain experienced is preserved in the microstructure (Supplementary Figure 4). Our simulations suggest when interpreting a shear zone, in addition to the aspects suggested by Means (1995), consideration should be given to the interaction of strengthening and weakening processes, as all parts of the shear zone may not have been active concurrently during the shear zone formation (simulation set IV). Under these circumstances the pre-existing weak component geometry may or may not be visible (Fig. 6). Where the pre-existing weak geometry is deformed, this suggests any strengthening processes may have been limited, similarly to our simulation sets II and III.

5. Conclusions

This study highlights the following for bulk material strength and shear zone formation: (1) IWLs are difficult to form without a dynamic weakening process. (2) Feedbacks causing rheological weakening with or without strengthening during deformation can quickly localize strain into an IWL, and it is possible for these to form from very low area percentages of original weak phase. (3) During widespread weakening, strain localises into increased numbers of interconnected IWLs, thereby increasing the anastomosing character of the shear zones. (4) Temporal patterns of shear zone activity are sensitive to the dominance of weakening or strengthening processes. (5) Shear zones are dynamic in time and space within a single deformation event; hence the pattern of finite strain can be an incomplete representation of the evolution of a shear zone network. The numerical model used is scale independent and hence these insights can be applied to strain localization at all scales.

ACKNOWLEDGEMENTS

Logistical and analytical funding was provided by an MQRes scholarship (RG), Future Fellowship (FT1101100070 to SP) and internal funding from the Department of Earth and Planetary Sciences, Macquarie University. The authors would also like to thank Christopher Gerbi and an anonymous reviewer for their careful and constructive reviews, and An Yin for editorial handling. This is contribution xxx from the ARC Centre of Excellence for Core to Crust Fluid Systems (http://www.ccfs.mq.edu.au) and xxx in the GEMOC Key Centre (http://www.gemoc.mq.edu.au).

REFERENCES

Arbaret, L., Burg, J.-P., Zeilinger, G., Chaudhry, N., Hussain, S., Dawood, H., 2000. Pre-collisional anastomosing shear zones in the Kohistan arc, NW Pakistan. Geological Society, London, Special Publications 170, 295-311.

Ashby, M.F., 1972. A first report on deformation-mechanism maps. Acta Metallurgica 20, 887-897.

Barnhoorn, A., Bystricky, M., Kunze, K., Burlini, L., Burg, J.-P., 2005. Strain localisation in bimineralic rocks: Experimental deformation of synthetic calcite–anhydrite aggregates. Earth and Planetary Science Letters 240, 748-763.

Bons, P.D., Koehn, D., Jessell, M.W., 2008. Microdynamics Modelling. Lecture Notes in Earth Sciences. Springer, Berlin.

Bouchot, V., Gros, Y., Bonnemaison, M., 1989. Structural controls on the auriferous shear zones of the Saint Yrieix District, Massif Central, France; evidence from the Le Bourneix and Laurieras gold deposits. Economic Geology 84, 1315-1327.

Brodhag, S.H., Herwegh, M., Berger, A., 2011. Grain coarsening in polymineralic contact metamorphic carbonate rocks: The role of different physical interactions during coarsening. Journal of Structural Geology 33, 698-712.

Carreras, J., 2001. Zooming on Northern Cap de Creus shear zones. Journal of Structural Geology 23, 1457-1486.

Carreras, J., Czeck, D.M., Druguet, E., Hudleston, P.J., 2010. Structure and development of an anastomosing network of ductile shear zones. Journal of Structural Geology 32, 656-666.

Chester, F.M., 1995. A rheologic model for wet crust applied to strike-slip faults. Journal of Geophysical Research: Solid Earth 100, 13007-13020.

Cook, A.C., Vel, S.S., Gerbi, C., Johnson, S.E., 2014. Computational analysis of nonlinear creep of polyphase aggregates: Influence of phase morphology. Journal of Geophysical Research: Solid Earth 119, 6877-6906.

Cross, A.J., Ellis, S., Prior, D.J., 2015. A phenomenological numerical approach for investigating grain size evolution in ductiley deforming rocks. Journal of Structural Geology 76, 22-34.

De Bresser, J., Ter Heege, J., Spiers, C., 2001. Grain size reduction by dynamic recrystallization: can it result in major rheological weakening? Int J Earth Sci (Geol Rundsch) 90, 28-45.

De Bresser, J.H.P., Peach, C.J., Reijs, J.P.J., Spiers, C.J., 1998. On dynamic recrystallization during solid state flow: Effects of stress and temperature. Geophysical Research Letters 25, 3457-3460.

Dell'Angelo, L.N., Tullis, J., 1996. Textural and mechanical evolution with progressive strain in experimentally deformed aplite. Tectonophysics 256, 57-82.

Drury, M.R., 2005. Dynamic recrystallization and strain softening of olivine aggregates in the laboratory and the lithosphere. Geological Society, London, Special Publications 243, 143-158.

Finch, M.A., Weinberg, R.F., Hunter, N.J.R., 2016. Water loss and the origin of thick ultramylonites. Geology 44, 599-602.
Fliervoet, T.F., White, S.H., Drury, M.R., 1997. Evidence for dominant grain-boundary sliding deformation in greenschist- and amphibolite-grade polymineralic ultramylonites from the Redbank Deformed Zone, Central Australia. Journal of Structural Geology 19, 1495-1520.
Gerbi, C., 2012. Evaluating the utility of a phase distribution parameter in calculating the bulk viscous strength of two-phase composites. Journal of Structural Geology 39, 224-236.
Gerbi, C., Johnson, S.E., Cook, A., Vel, S.S., 2015. Effect of phase morphology on bulk strength for power-law materials. Geophysical Journal International 200, 374-389.
Gerbi, C., Johnson, S.E., Shulman, D., Klepeis, K., 2016. Influence of microscale weak zones on bulk strength. Geochemistry, Geophysics, Geosystems 17, 4064-4077.
Handy, M.R., 1994. Flow laws for rocks containing two non-linear viscous phases: A phenomenological approach. Journal of Structural Geology 16, 287-301.
Hanmer, S., 1988. Great Slave Lake Shear Zone, Canadian Shield: reconstructed vertical profile of a crustal-scale fault zone. Tectonophysics 149, 245-264.
Hansen, L.N., Zimmerman, M.E., Dillman, A.M., Kohlstedt, D.L., 2012. Strain localization in olivine aggregates at high temperature: A laboratory comparison of constant-strain-rate and constant-stress boundary conditions. Earth and Planetary Science Letters 333–334, 134-145.
Herwegh, M., Berger, A., 2004. Deformation mechanisms in second-phase affected microstructures and their energy balance. Journal of Structural Geology 26, 1483-1498.
Herwegh, M., Poulet, T., Karrech, A., Regenauer-Lieb, K., 2014. From transient to steady state deformation and grain size: A thermodynamic approach using elasto-visco-plastic numerical modeling. Journal of Geophysical Research: Solid Earth 119, 900-918.
Hobbs, B., Regenauer-Lieb, K., Ord, A., 2008. Folding with thermal–mechanical feedback. Journal of Structural Geology 30, 1572-1592.
Holyoke III, C.W., Tullis, J., 2006. Mechanisms of weak phase interconnection and the effects of phase strength contrast on fabric development. Journal of Structural Geology 28, 621-640.
Houseman, G.A., Barr, T.D., Evans, L., 2008. Basil: stress and deformation in a viscous material, in: Bons, P.D., Koehn, D., Jessell, M.W. (Eds.), Microdynamics Simulation. Lecture Notes in Earth Sciences. Springer, Berlin, p. 405.
Jessell, M., Bons, P., Evans, L., Barr, T., Stüwe, K., 2001. Elle: the numerical simulation of metamorphic and deformation microstructures. Computers & Geosciences 27, 17-30.
Jessell, M.W., Bons, P.D., Griera, A., Evans, L.A., Wilson, C.J.L., 2009. A tale of two viscosities. Journal of Structural Geology 31, 719-736.
Jessell, M.W., Siebert, E., Bons, P.D., Evans, L., Piazolo, S., 2005. A new type of numerical experiment on the spatial and temporal patterns of localization of deformation in a material with a coupling of grain size and rheology. Earth and Planetary Science Letters 239, 309-326.
Llorens, M.-G., Griera, A., Bons, P.D., Roessiger, J., Lebensohn, R., Evans, L., Weikusat, I., 2016. Dynamic recrystallisation of ice aggregates during co-axial

viscoplastic deformation: a numerical approach. Journal of Glaciology FirstView, 1-19.

Mancktelow, N.S., 2002. Finite-element modelling of shear zone development in viscoelastic materials and its implications for localisation of partial melting. Journal of Structural Geology 24, 1045-1053.

Means, W.D., 1995. Shear zones and rock history. Tectonophysics 247, 157-160.

Montési, L.G.J., 2013. Fabric development as the key for forming ductile shear zones and enabling plate tectonics. Journal of Structural Geology 50, 254-266.

Piazolo, S., Bons, P.D., Jessell, M.W., Evans, L., Passchier, C.W., 2002. Dominance of microstructural processes and their effect on microstructural development: insights from numerical modelling of dynamic recrystallization. Geological Society, London, Special Publications 200, 149-170.

Piazolo, S., Jessell, M.W., Bons, P.D., Evans, L., Becker, J.K., 2010. Numerical simulations of microstructures using the Elle platform: A modern research and teaching tool. Journal of the Geological Society of India 75, 110-127.

Platt, J.P., 2015. Influence of shear heating on microstructurally defined plate boundary shear zones. Journal of Structural Geology 79, 80-89.

Poulet, T., Veveakis, M., Herwegh, M., Buckingham, T., Regenauer-Lieb, K., 2014. Modeling episodic fluid-release events in the ductile carbonates of the Glarus thrust. Geophysical Research Letters 41, 7121-7128.

Rennie, S.F., Fagereng, Å., Diener, J.F.A., 2013. Strain distribution within a km-scale, mid-crustal shear zone: The Kuckaus Mylonite Zone, Namibia. Journal of Structural Geology 56, 57-69.

Rybacki, E., Dresen, G., 2004. Deformation mechanism maps for feldspar rocks. Tectonophysics 382, 173-187.

Segall, P., Simpson, C., 1986. Nucleation of ductile shear zones on dilatant fractures. Geology 14, 56-59.

Shea, W.T., Kronenberg, A.K., 1993. Strength and anisotropy of foliated rocks with varied mica contents. Journal of Structural Geology 15, 1097-1121.

Smith, J., Piazolo, S., Daczko, N., Evans, L., 2015. The effect of pre-tectonic reaction and annealing extent on behaviour during subsequent deformation: Insights from paired shear zones in the lower crust of Fiordland, New Zealand. Journal of Metamorphic Geology 33, 557-670.

Svahnberg, H., Piazolo, S., 2010. The initiation of strain localisation in plagioclase-rich rocks: Insights from detailed microstructural analyses. Journal of Structural Geology 32, 1404-1416.

Takeda, Y.-T., Griera, A., 2006. Rheological and kinematical responses to flow of two-phase rocks. Tectonophysics 427, 95-113.

Treagus, S.H., 2002. Modelling the bulk viscosity of two-phase mixtures in terms of clast shape. Journal of Structural Geology 24, 57-76.

Tullis, T.E., Horowitz, F.G., Tullis, J., 1991. Flow laws of polyphase aggregates from end-member flow laws. Journal of Geophysical Research: Solid Earth 96, 8081-8096.

Twiss, R., 1977. Theory and Applicability of a Recrystallized Grain Size Paleopiezometer, in: Wyss, M. (Ed.), Stress in the Earth. Birkhäuser Basel, pp. 227-244.

Warren, J.M., Hirth, G., 2006. Grain size sensitive deformation mechanisms in naturally deformed peridotites. Earth and Planetary Science Letters 248, 438-450.

Figure Labels

Figure 1. (a) Geometries used in the numerical models. (i) Base polygon mesh; (ii)-(vi) load bearing framework geometries with 20% weak component: (ii) horizontal stripes (iii) vertical stripes (iv) random (v) cluster and (vi) ring geometries. Pink is weak component (η^* = 1; n = 1); brown is strong component (η^* = 5; n = 3). (b) Generic deformation mechanism map of grain size vs shear stress showing the transition between dislocation creep and diffusion creep/GBS for two notional temperature/shear strain rate pairs. Simulation set II models weakening transition to diffusion creep/GBS along a single contour (red arrow, lower contour). Simulation set III models this transition along multiple contours, as defined by σ_{Thr} (red arrows). Simulation set IV models the weakening transition to diffusion creep/GBS and the strengthing transition to dislocation creep on multiple contours, as defined by σ_{Thr} and A_{Thr} (red and blue arrows). (c and d) Schematic flow diagram for dynamic feedback processes; (c) weakening process only, used in simulation sets II and III; (d) weakening and strengthening processes, used in simulation set IV. η^* is viscosity pre-factor, n is stress exponent, σ_{Incr} is incremental stress, σ_{Thr} is stress threshold, A_{Thr} is age threshold (for details see text), NC is no change.

Figure 2. Variation of material strength for tested geometries during progressive deformation. (a) Simulation set I: material strength of geometries with no rheological feedback: Newtonian flow (n = 1; solid lines), non-Newtonain flow (n = 3; dashed lines) and mixed flow regime, i.e., Newtonian (n = 1) for weak polygons and non-Newtonian (n = 3) for strong polygons (dotted lines); vertical striped geometry insets show rotation of stripes with initially increasing, then decreasing strength. (b)

Simulation set II: Material strength of geometries when dynamic rheological weakening is activated; mixed Newtonian and non-Newtonian flow regime: Vertical striped geometry insets show initial increase in strength then sharp decrease as an IWL forms.

Figure 3. Impact of initial geometry and dynamic rheological weakening on pattern of strain localization during progressive deformation; simulation set II: dynamic weakening with σ_{Thr} = 6.0. Incremental and accumulated strain for (a) horizontal stripes, (b) vertical stripes, (c) cluster (d) ring and (e) random geometries at γ of 1 and 2. Incremental strain plots use values from the node grid, while accumulated strain plots show the node grid; red lines were originally horizontal, grey lines were vertical connecting the nodes in a grid. X-axis of incremental and accumulated strain graphs is the integral of the strain values across the grid at that Y axis position. Peaks in the graphs show location of strain concentration; bars on right are a proxy for IWL width for γ of 1 (blue) and γ of 2 (red); showing width of zone where the strain integral is greater than 1 (marked by the dotted line).

Figure 4. Impact of dynamic rheological weakening threshold on material strength during progressive deformation; simulation set III: (a) material strength of each cluster geometry; (b) percentage of strong component in the model. All models initially start with LBF, at 80% strong areas (that is, 20% weak areas).

Figure 5: Impact of dynamic rheological weakening threshold on pattern of strain localization during progressive deformation; simulation set III: Images of viscosity

pre-factor (η^*; based on polygon geometry) and accumulated strain (from the Layer 2 unconnected node values) taken at γ of 1 and 2 showing the resulting weak and strong phases and strain localisation. X-axis of accumulated strain graphs is the integral of the strain values across the grid at that Y axis position. Peaks in the graphs show location of strain concentration; bars on right are a proxy for IWL width for γ of 1 (blue) and γ of 2 (red); showing width of zone where the strain integral is greater than 1 (marked by the dotted line); * γ of 2 bars are shown, however, an IWL was not formed.

Figure 6. Summary of the impact of increasing weakening and strengthening processes on IWL formation; plots of accumulated strain at γ of 2; simulation set IV where A_{Thr} is specified, set III where no A_{Thr} is set; as more weakening occurs, IWLs increase in number and become interconnected; as more strengthening occurs IWLs decrease in number; * denotes a movie of the simulation is available in the Supplementary material.

Figure 7. Impact of dynamic rheological weakening and strengthening on pattern of strain localization during progressive deformation; simulation set IV; (a) incremental and accumulated strain plots at σ_{Thr} of 5.0 for (i) $A_{Thr} = 5$, (ii) $A_{Thr} = 10$, (iii) $A_{Thr} = 15$, (iv) $A_{Thr} = 20$ from Layer 2 unconnected node values. Incremental strain plots show strain varies with time (black arrow pairs). Peaks in the graphs show location of strain concentration; bars on right are a proxy for IWL width for γ of 1 (blue) and γ of 2 (red); showing width of zone where the strain integral is greater than 1 (marked by the dotted line). (b) Areas shown have experienced an incremental strain $\varepsilon_{Incr} > 0.06$

for σ_{Thr} = 5.0 and A_{Thr} = 10. For clarity three groups of different strain (γ) intervals are shown. (i) γ of 0.125 to 0.625, (ii) γ of 0.875 to 1.375 and (iii) γ of 1.625 to 2.125. The strain is heterogeneous in the IWL at a given shear strain. Locus of high strain moves with time (compare locations between γ values). See text for details.

Figure 8. Impact of dynamic rheological weakening and strengthening (σ_{Thr} and A_{Thr}) on material strength; simulation set IV: starting geometry is cluster geometry with random age (between 0 and A_{Thr}) set after initial weakening; see text for details. (a) σ_{Thr} = 4.0 (weak phase supporting, see Fig.5), (b) σ_{Thr} = 5.0 (load bearing framework, see Fig.5) and (c) σ_{Thr} = 6.0 (load bearing framework, see Fig.5).

Figure 9. Formation of an IWL from very few weak polygons; simulation set IV. Both starting weak component geometries at gamma of 0 are the same, however, slight variations in dynamic weakening and deformation occur during the model run; both (a) and (b) are of incremental strain from σ_{Thr} = 6.0, A_{Thr} = 5 where all initial ages are 0. (a) An IWL is initiated from 0.74% weak phase by γ = 0.3; (b) no IWL forms.

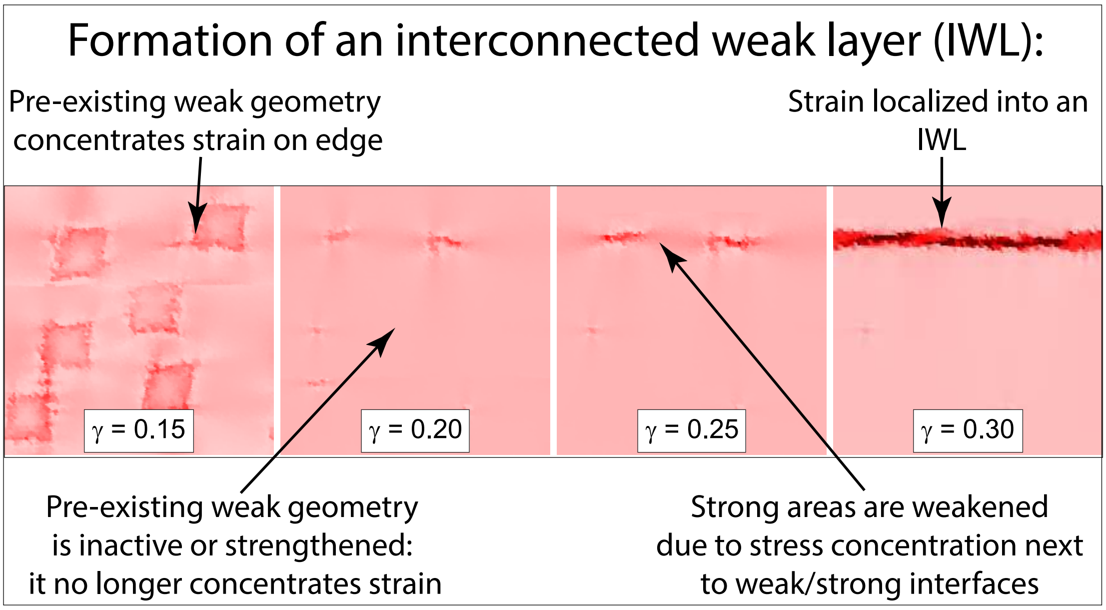

Graphical Abstract

Figure

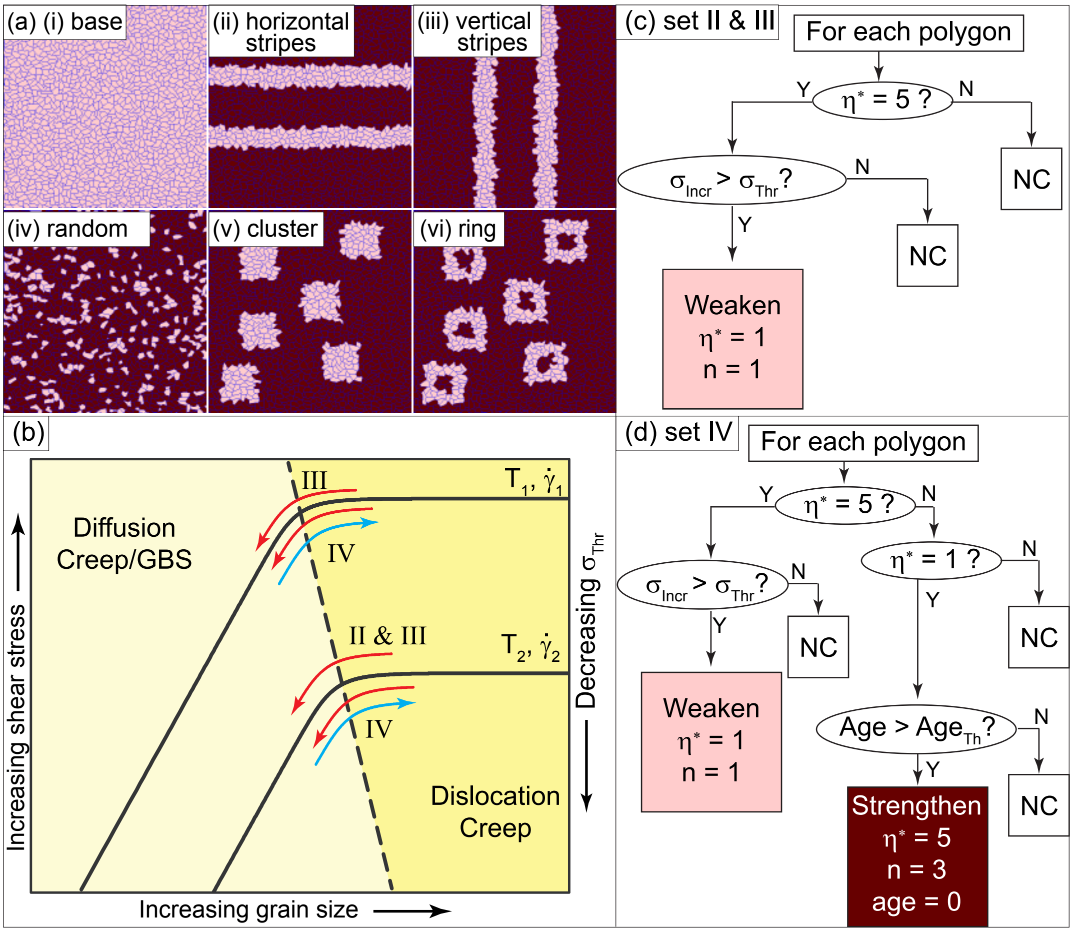

Figure 1. (a) Geometries used in the numerical models. (i) Base polygon mesh; (ii)-(vi) load bearing framework geometries with 20% weak component: (ii) horizontal stripes (iii) vertical stripes (iv) random (v) cluster and (vi) ring geometries. Pink is weak component ($\eta^* = 1$; $n = 1$); brown is strong component ($\eta^* = 5$; $n = 3$). (b) Generic deformation mechanism map of grain size vs shear stress showing the transition between dislocation creep and diffusion creep/GBS for two notional temperature/shear strain rate pairs. Simulation set II models weakening transition to diffusion creep/GBS along a single contour (red arrow, lower contour). Simulation set III models this transition along multiple contours, as defined by σ_{Thr} (red arrows). Simulation set IV models the weakening transition to diffusion creep/GBS and the strengthing transition to dislocation creep on multiple contours, as defined by σ_{Thr} and A_{Thr} (red and blue arrows). (c and d) Schematic flow diagram for dynamic feedback mechanisms; (c) weakening mechanism only, used in simulation sets II and III; (d) weakening and strengthening mechanisms, used in simulation set IV. η^* is viscosity pre-factor, n is stress exponent, ε_{Incr} is incremental stress, σ_{Thr} is stress threshold, A_{Thr} is age threshold (for details see text), NC is no change.
(2 columns)

Figure

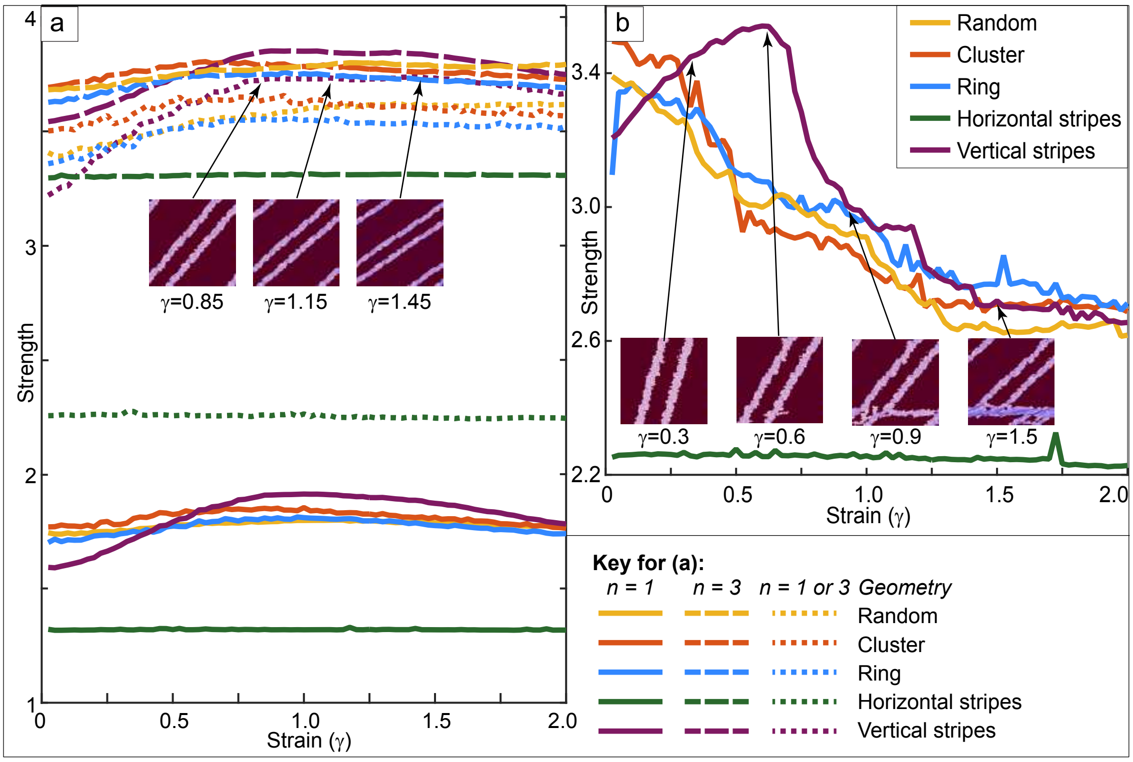

Figure 2. Variation of material strength for tested geometries during progressive deformation. (a) Simulation set I: material strength of geometries with no rheological feedback: Newtonian flow (n = 1; solid lines), non-Newtonain flow (n = 3; dashed lines) and mixed flow regime, i.e., Newtonian (n = 1) for weak polygons and non-Newtonian (n = 3) for strong polygons (dotted lines); vertical striped geometry insets show rotation of stripes with initially increasing, then decreasing strength. (b) Simulation set II: Material strength of geometries when dynamic rheological weakening is activated; mixed Newtonian and non-Newtonian flow regime: Vertical striped geometry insets show initial increase in strength then sharp decrease as an IWL forms.
(2 columns)

Figure

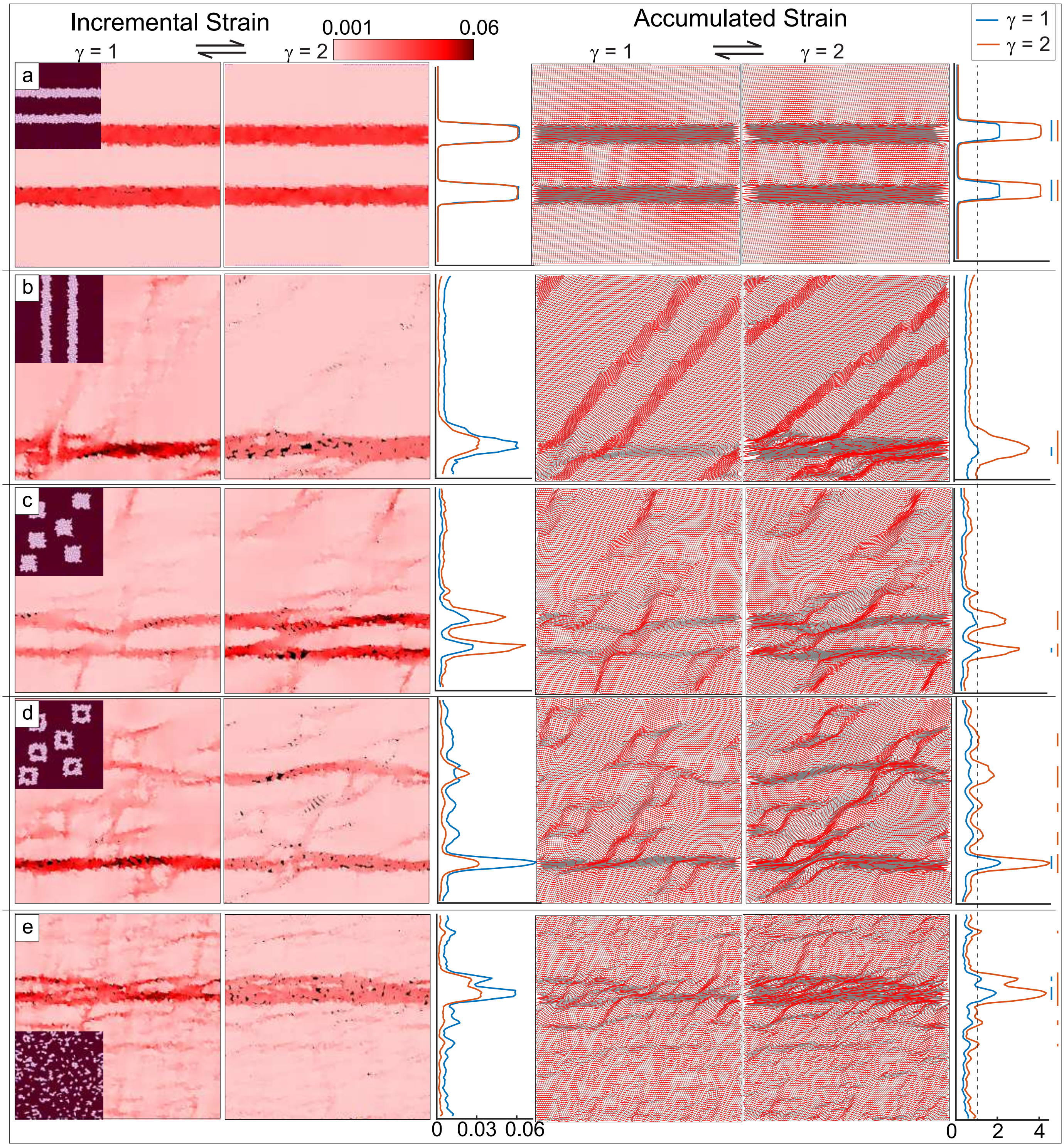

Figure 3. Impact of initial geometry and dynamic rheological weakening on pattern of strain localization during progressive deformation; simulation set II: dynamic weakening with σ_{Thr} = 6.0. Incremental and accumulated strain for (a) horizontal stripes, (b) vertical stripes, (c) cluster (d) ring and (e) random geometries at γ of 1 and 2. Incremental strain plots use values from the node grid, while accumulated strain plots show the node grid; red lines were originally horizontal, grey lines were vertical connecting the nodes in a grid. X-axis of incremental and accumulated strain graphs is the integral of the strain values across the grid at that Y axis position. Peaks in the graphs show location of strain concentration; bars on right are a proxy for IWL width for γ of 1 (blue) and γ of 2 (red); showing width of zone where the strain integral is greater than 1 (marked by the dotted line).
(2 columns)

Figure

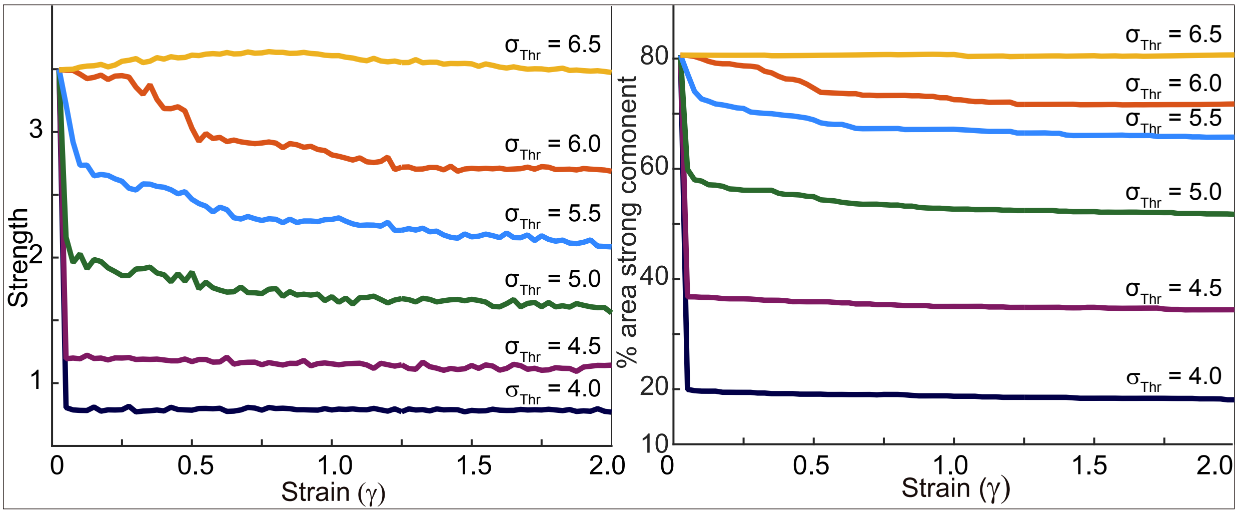

Figure 4. Impact of dynamic rheological weakening threshold on material strength during progressive deformation; simulation set III: (a) material strength of each cluster geometry; (b) percentage of strong component in the model. All models initially start with LBF, at 80% strong areas (that is, 20% weak areas).

(2 columns)

Figure

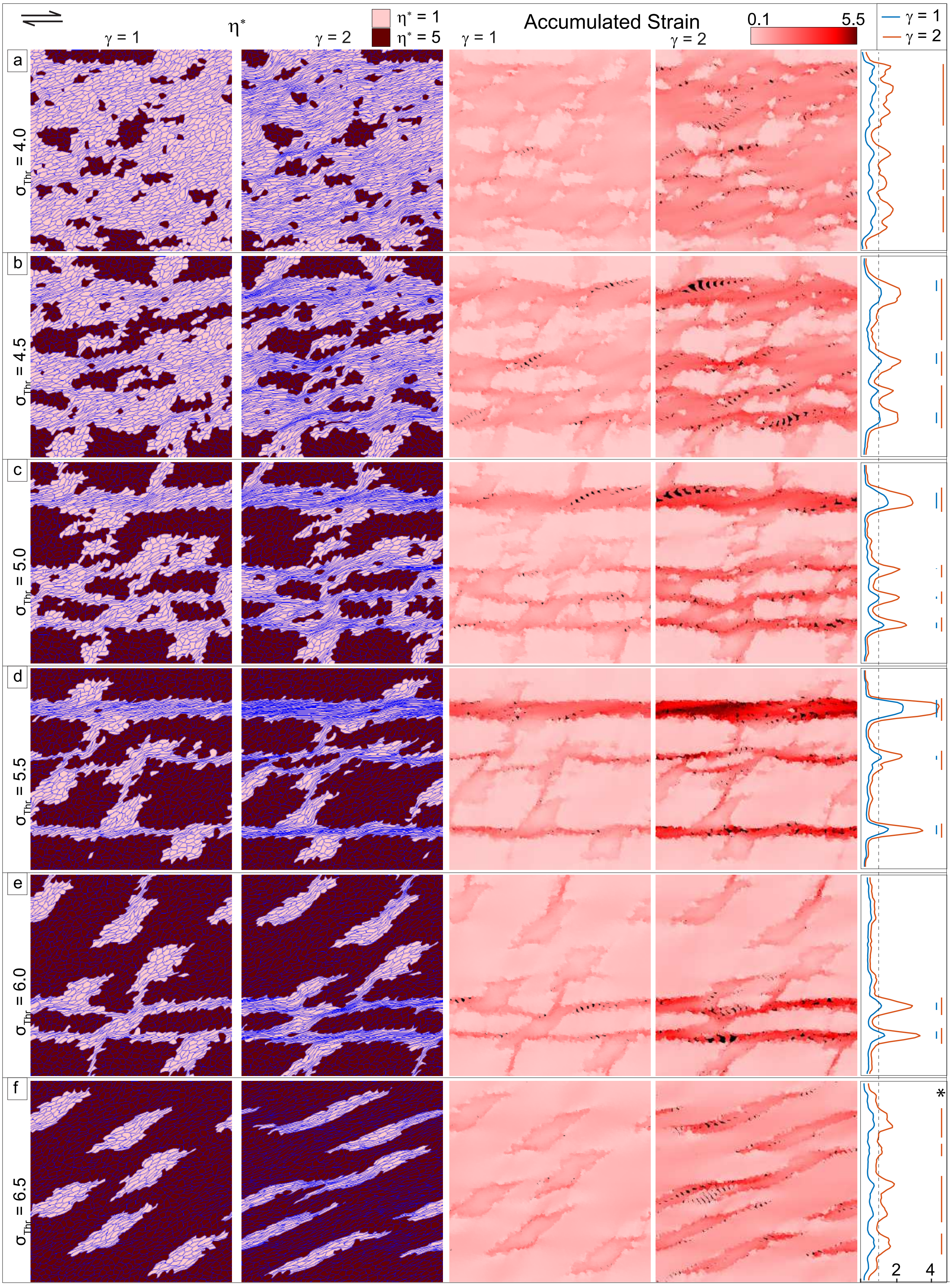

Figure 5: Impact of dynamic rheological weakening threshold on pattern of strain localization during progressive deformation; simulation set III: Images of viscosity pre-factor (η^* based on polygon geometry) and accumulated strain (from unconnected node values) taken at γ of 1 and 2 showing the resulting weak and strong phases and strain localisation. X-axis of accumulated strain graphs is the integral of the strain values across the grid at that Y axis position. Peaks in the graphs show location of strain concentration; bars on right are a proxy for IWL width for γ of 1 (blue) and γ of 2 (red); showing width of zone where the strain integral is greater than 1 (marked by the dotted line); * γ of 2 bars are shown, however, an IWL was not formed.
(2 columns)

Figure

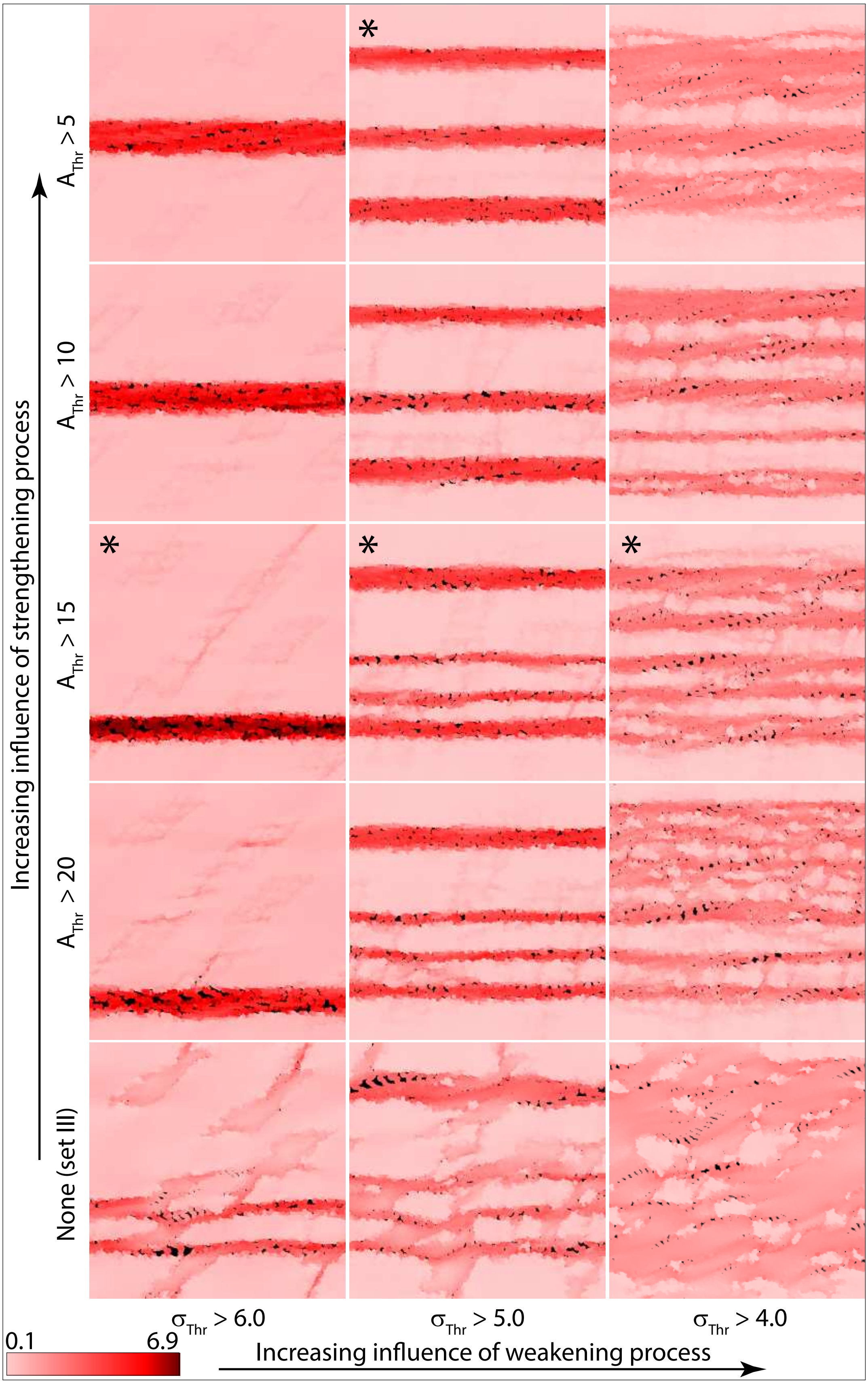

Figure 6. Summary of the impact of increasing weakening and strengthening processes on IWL formation; plots of accumulated strain at γ of 2; simulation set IV where A_{Thr} is specified, set III where no A_{Thr} is set; as more weakening occurs, IWLs increase in number and become interconnected; as more strengthening occurs IWLs decrease in number; * denotes a movie of the simulation is available in the Supplementary material.

Figure

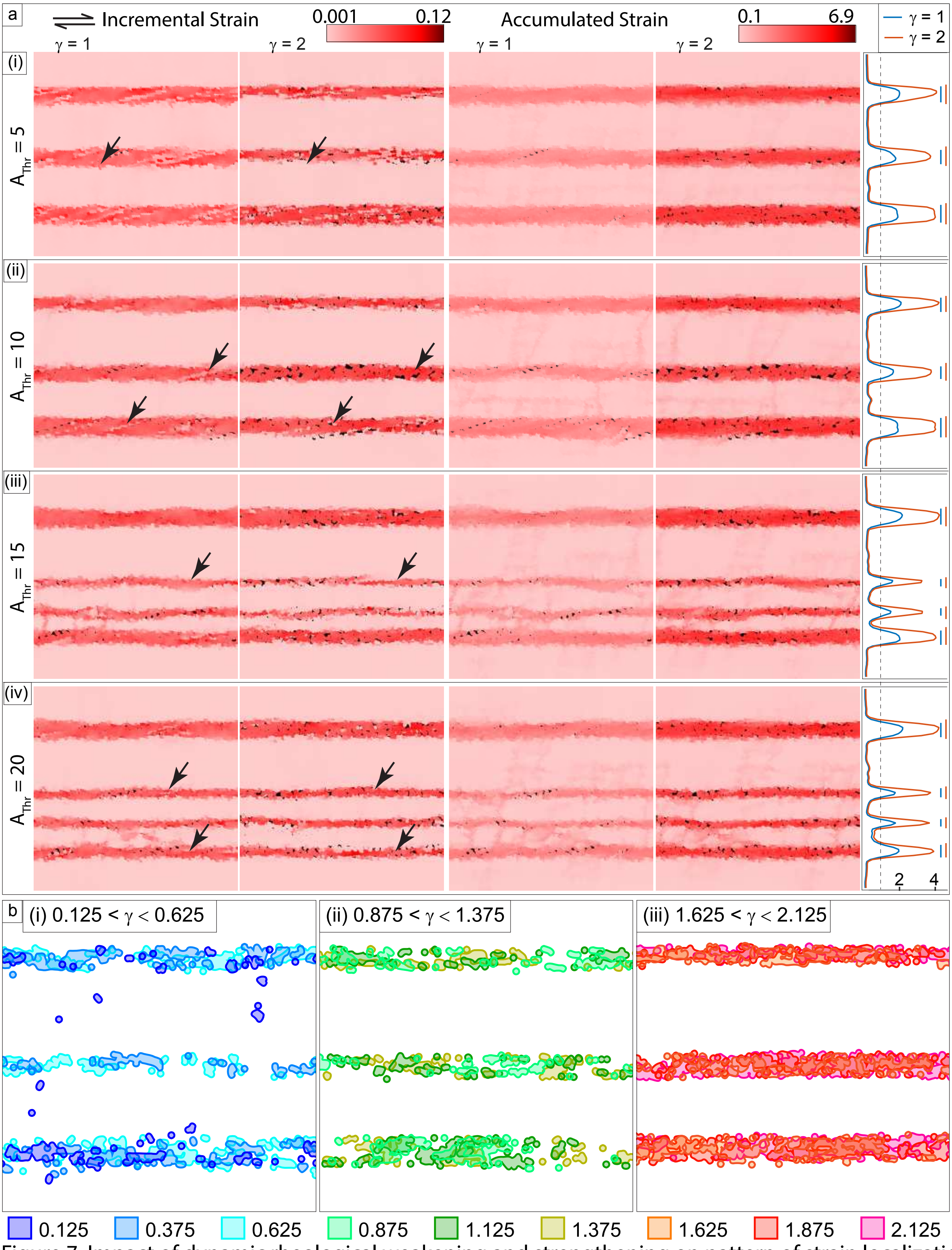

Figure 7. Impact of dynamic rheological weakening and strengthening on pattern of strain localization during progressive deformation; simulation set IV; (a) incremental and accumulated strain plots at σ_{Thr} of 5.0 for (i) $A_{Thr} = 5$, (ii) $A_{Thr} = 10$, (iii) $A_{Thr} = 15$, (iv) $A_{Thr} = 20$ from unconnected node values. Incremental strain plots show strain varies with time (black arrow pairs). Peaks in the graphs show location of strain concentration; bars on right are a proxy for IWL width for γ of 1 (blue) and γ of 2 (red); showing width of zone where the strain integral is greater than 1 (marked by the dotted line). (b) Areas shown have experienced an incremental strain $\varepsilon_{Incr} > 0.06$ for $\sigma_{Thr} = 5.0$ and $A_{Thr} = 10$. For clarity three groups of different strain (γ) intervals are shown. (i) γ of 0.125 to 0.625, (ii) γ of 0.875 to 1.375 and (iii) γ of 1.625 to 2.125. The strain is heterogeneous in the IWL at a given shear strain. Locus of high strain moves with time (compare locations between γ values). See text for details.
(2 columns)

Figure

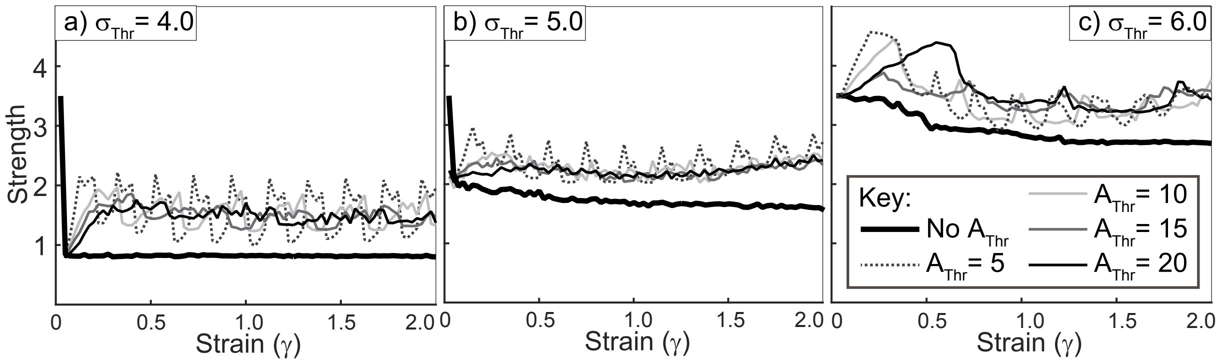

Figure 8. Impact of dynamic rheological weakening and strengthening (σ_{Thr} and A_{Thr}) on material strength; simulation set IV: starting geometry is cluster geometry with random age (between 0 and A_{Thr}) set after initial weakening; see text for details. (a) σ_{Thr} = 4.0 (weak phase supporting, see Fig.5), (b) σ_{Thr} = 5.0 (load bearing framework, see Fig.5) and (c) σ_{Thr} = 6.0 (load bearing framework, see Fig.5).
(2 columns)

Figure

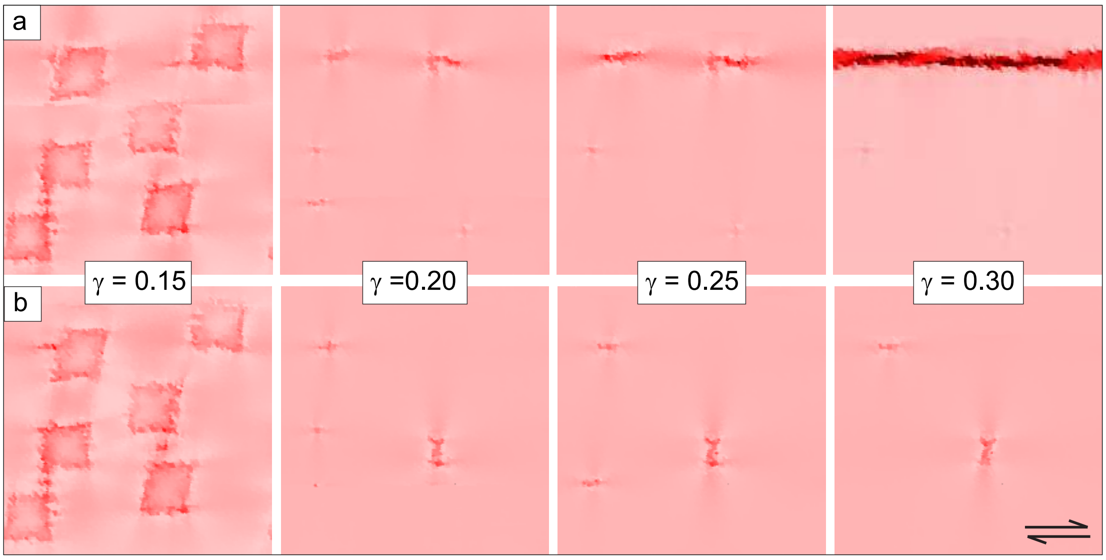

Figure 9. Formation of an IWL from very few weak polygons; simulation set IV. Both starting weak component geometries at gamma of 0 are the same, however, slight variations in dynamic weakening and deformation occur during the model run; both (a) and (b) are of incremental strain from $\sigma_{Thr} = 6.0$, $A_{Thr} = 5$ where all initial ages are 0. (a) An IWL is initiated from 0.74% weak phase by $\gamma = 0.3$; (b) no IWL forms.
(2 columns)